Numerical Study of the Magnetorotational Instability in Princeton MRI Experiment

Wei Liu[1]

Center for Magnetic Self-Organization in Laboratory and Astrophysical Plasma, Princeton Plasma Physics Laboratory, Princeton, NJ, USA 08543

`wliu@lanl.gov`

Abstract

In preparation for an experimental study of magnetorotational instability (MRI) in liquid metal, we present non-ideal axisymmetric magnetohydrodynamic simulations of the nonlinear evolution of MRI in the experimental geometry. The simulations adopt fully insulating boundary conditions. No-slip conditions are imposed at all boundaries. A clear linear phase is observed with reduced linear growth rate. MRI results in an inflowing "jet" near the midplane and enhances the angular momentum transport at saturation.

Subject headings: accretion, accretion disks — instabilities — methods: numerical — MHD

1. Introduction

The magnetorotational instability (MRI) is probably the main cause of turbulence and accretion in sufficiently ionized astrophysical disks (Balbus & Hawley 1998), which has inspired searches for MRI in Taylor-Couette flow. Experiments on magnetized Couette flow aiming to observe MRI have been performed (Sisan et al. 2004; Stefani et al. 2006). Those experiments have demonstrated MRI-like modes, but not yet for background flows that approximate Keplerian disks. Sisan et al. (2004) observed nonaxisymmetric modes and enhanced transport in a spherical experiment, but with a hydrodynamically linearly unstable background state. Stefani et al. (2006); Rüdiger et al. (2006); Stefani et al. (2007) demonstrated unsteady behavior in a very low-Rm experiment with a strong toroidal as well as axial

---

[1]current address: Theoretical Division, Los Alamos National Laboratory, Los Alamos, NM, USA 87545

field; the relationship between the experimental results and linear instabilities is still controversial (Liu et al. 2006a; Priede et al. 2007; Liu et al. 2007; Rüdiger & Hollerbach 2007; Szklarski 2007; Liu 2008a), but if these are indeed the linear modes, then the corresponding ratio of toroidal to axial field in a thin (thickness $\Delta h \ll r$) disk would have to be $\sim r/\Delta h$, where r is the radius of the accretion disk. Some other experiments have been proposed or are still under construction (Noguchi et al. 2002; Velikhov et al. 2006; Ji et al. 2001; Goodman & Ji 2002).

Standard MRI modes will not grow unless both the rotation period and the Alfvén crossing time are shorter than the timescale for magnetic diffusion. This requires that both the magnetic Reynolds number $Re_{\rm m} \equiv \Omega_1 r_1 (r_2 - r_1)/\eta_{\rm Ga}$ (see definitions of Ω_1, $\eta_{\rm Ga}$, r_1 and r_2 in Fig. 1 and their values in Table. 1) and the Lundquist number $S \equiv V_{Az}^0 (r_2 - r_1)/\eta_{\rm Ga}$ be $\gtrsim 1$, where $V_{Az}^0 = B_\infty/\sqrt{4\pi\rho_{\rm Ga}}$ is the Alfvén speed, $\rho_{\rm Ga}$ is the density of liquid Gallium and B_∞ is the background magnetic field parallel to the angular velocity. Because the magnetic Prandtl number $Pr_{\rm m} \equiv \nu/\eta \sim 10^{-5} - 10^{-6}$ in liquid metals, where $\nu_{\rm Ga}$ is the kinematic viscosity of liquid gallium, $Re \gtrsim 10^6$ and fields of several kilogauss for standard MRI must be achieved in typical experimental geometries. Recent linear analyses have shown that MRI-like mode could grow with much reduced magnetic Reynolds number and Lundquist number in the presence of a helical background magnetic field (Hollerbach & Rüdiger 2005; Rüdiger et al. 2005), at least for cylinders of infinite or periodic axial extent (Liu et al 2006b). The simulations of this paper, however, are limited to axial background fields

The experiment is complicated by the large ($\gtrsim 10^6$) Reynolds number and by Ekman circulation and Stewartson layers (Hollerbach & Fournier 2004), even though the Princeton MRI experimental apparatus has been constructed to minimize the circulation by the use of independently controlled split endcaps (Kageyama et al. 2004; Burin et al. 2006; Ji et al. 2006). It is known that Ekman circulation is significantly modified when the Elsasser number Λ exceeds unity: $\Lambda = B_\infty^2/(8\pi\rho_{\rm Ga}\eta_{\rm Ga}\bar{\Omega}) \gtrsim 1$ where $\bar{\Omega} = \sqrt{\Omega_1\Omega_2}$ is the characteristic rotation frequency (Gilman 1971). At 100% of the maximum designed rotation rate of our experiment (Table.1) and with $I_\varphi = 1000$ A, where I_φ is the external coil current (Fig. 1), the Elsasser number $\Lambda = 0.36$.

There have been few published studies of the nonlinear saturation of MRI in an experimental Taylor-Couette geometry apart from Knobloch & Julien (2005); Liu et al. (2006b); Umurhan et al. (2007b,a), and even fewer with realistic experimental boundary conditions. As noted in Liu et al. (2006b), the nature of saturation of MRI in a Couette flow is essentially different from accretion disks, in which MRI is believed to saturate by turbulent reconnection (Fleming et al. 2000; Sano & Inutsuka 2001). In accretion disks, differential rotation arises from a balance between the gravitational attraction of the accreting body

and centrifugal force. Thermal and turbulent energies are probably small compared to orbital ones, so saturation is not likely to occur by modification of the mean flow profile. In experiments, however, differential rotation is imposed by viscous or other weak forces, so that mildly nonlinear MRI might well change the mean rotation profile.

This paper is the second of a series, following Liu et al. (2006b). Several idealizations made in that paper, notably the vertically periodic boundary conditions, are dispensed with here. We discuss the linear phase and nonlinear saturation of MRI in finite cylinders with realistic fluid and magnetic boundary conditions. All simulations reported here were performed with the ZEUS-MP 2.0 code (Hayes et al. 2006), which is a time-explicit, compressible, astrophysical ideal MHD parallel 3D code, to which we have added viscosity, resistivity (with subcycling to reduce the cost of the induction equation) for axisymmetric flows in cylindrical coordinates (r, φ, z) (Liu et al. 2006b). The implementation of fully insulating and partially conducting boundary conditions are discussed in Liu et al. (2007). The computational domain is shown in Fig. 1 and the parameters are summarized in Table 1. Six coils with dimensions as shown were used, with 67 turns in the two coils nearest the midplane and 72 in the rest. They are split into two sets of three in parallel, with the upper three in series and the bottom three also in series. Currents I_φ were adjusted according to the experimental values. Note that in the simulations the magnetic diffusivity η_{Ga} is fixed to the experimental value $\eta_{\mathrm{Ga}} = 2,430$ cm^2 s^{-1} (Table.1), however the kinematic viscosity is varied for the purpose of extrapolation from numerically tractable to experimentally realistic Reynolds numbers.

The measured current waveform is displayed in Fig. 2 for target currents of 1000 A and 400 A. The waveform displayed has an overshoot at the early stage, a linear decline and then a linear ramp where the controller tries to adjust the output voltage to reach the programmed set point. This behavior is peculiar to the high current runs (left panel of Fig. 2). Lower currents have a much flatter waveform (right panel of Fig. 2). In the simulation a wave form like that in Fig. 3 is used to approximate the experimental coil currents with ramp time $t_{\mathrm{coil}} = 0.2$ s.

Since the container is made of stainless steel, not a perfectly insulator, the radial magnetic angular momentum flux $(-rB_\varphi B_r/4\pi)$ at the cylinders need not vanish. In principle, the magnetic coupling of the fluid to the cylinders might modify the growth of the instability(Liu et al. 2007).

Fortunately, at the frequencies relevant to Princeton MRI experiment (100% run, $\bar{\Omega} = \sqrt{\Omega_1 \Omega_2} \sim 150\,\mathrm{Hz}$) the skin depth of stainless steel $\delta_w = \sqrt{2/\sigma_{\mathrm{Steel}} \bar{\Omega} \mu_0} \approx 9\,\mathrm{cm}$ (σ_{Steel} is the conductivity of stainless steel, see the value in Table. 1), which is much larger than the thickness of the steel vessel surrounding the gallium in the experiment, $d_w \approx 1.0\,\mathrm{cm}$,

so that the magnetic field diffuses rather easily into the boundary. If one considers axial currents, the gallium and the steel wall act as resistors in parallel; taking into account their conductivities and radial thicknesses, one finds that the resistances of steel walls are much larger than the resistance of the liquid gallium [$R_I : R_{II} : R_{III} = 65 : 1 : 21$; see Fig. 1 for the subscripts]. Therefore, the currents carried by the steel walls can be neglected for the toroidal field, so that the $B_r B_\varphi$ stress at the boundary is expected to be unimportant and an insulating boundary condition suffices.

The linear growth rate and saturated final state based on partially conducting boundary condition differs slightly from the results based on perfectly insulating boundary condition with partially conducting walls, which verifies our argument. Hereafter we ignore the conductivity of the stainless steel walls, but regard them as insulating materials, that is: $\eta_I = \eta_{II} = \infty$. Please note that in this whole paper the rotation profile used is $[\Omega_1, \Omega_2, \Omega_3, \Omega_4] = [4000, 533, 1820, 650]$ rpm (100% run, $\Omega_4 > \Omega_2$, Ω_1, Ω_2, Ω_3, and Ω_4 are the rotation speed of the inner cylincer, outer cylinder, inner ring and outer ring, respectively) (Table.1), under which the simulations predict that the bulk flow is almost ideal Couette state (Kageyama et al. 2004). And this is the desired basic state for MRI to grow. However, the experimental scans find that only if we choose $[\Omega_1, \Omega_2, \Omega_3, \Omega_4] = [400, 53, 146, 40]$ rpm (10% run, $\Omega_4 < \Omega_2$), the bulk flow profile is found to be very close to the ideal Couette state with the deviation (the boundary layer) highly confined near both endcaps (Ji et al. 2006). Ji et al. (2006) also shows that non-magnetic quasi-keplerian flows at Reynolds numbers up to millions are essentially steady, if the boundary effects have been properly considered. The Stewartson layer at the junction of the rings may be smoothed by localized circulation and/or turbulence from these instabilities (Liu 2008a). The rotation profile to be used in the magnetized runs would be $[\Omega_1, \Omega_2, \Omega_3, \Omega_4] = [2400, 320, 876, 240]$ rpm (60% run, $\Omega_4 < \Omega_2$). The difference of the rotation profile at the end caps between in the experiment and in the simulation could possibly be explained by the wobbling of the inner cylinder in the experimental runs due to the difficulties of aligning the inner cylinder perfectly and the gaps between the rings and cylinders (Roach et al. 2007). And these effects are speculated to be more important with higher Reynolds number $Re \sim 10^6 - 10^7$ as in the experiment. Unfortunately, the modern computers and codes can not afford a simulation with Reynolds number as high as several million. Although this is not experimentally realizable, the low-Reynolds-number results reported in this paper without wobbling, gaps and starting from an initially ideal Couette state with fully insulating magnetic boundary conditions still gives us some useful hints about what is going on in the experiment. The result maybe is even closer to what is happening in the experiment based on the purely hydrodynamic experiment (steady flow, mostly ideal Couette state in the bulk), although this argument needs to be proven. We are addressing the problem step by step, adding the complexity into the code one by one. To

include all subtle points at one time would perplex the problem and make it difficult for us to catch the essence of the problem. The detailed study of the influence of the wobbling and gaps between the rings is on the way to investigate the discrepancies between the experimental results and simulations. Also we want to point out: as demonstrated by Goodman & Ji (2002), the viscosity of liquid metals is so small as to be almost irrelevant to MRI, at least in the linear regime. Thus a low-Reynolds-number run would be fine, at least in this sense.

Most of results presented in this paper are the results of 100% run except stated explicitly. The simulation results have proved very valuable in design, operation and understanding of the experiment. The outline of this paper is as follows. We present the results of the linear MRI in Sec. 2. And the results of the nonlinear saturation of MRI are discussed in Sec. 3. Sec. 4 summarizes the results and presents the final conclusions.

2.   Linear Phase

2.1.   Linear Growth Rate Reduced by the Residual Magnetized Ekman Circulation

The first convincing evidence of the existence of MRI is its linear growth rate (Fig. 4). We find this linear growth rate is reduced from 33.1 s^{-1} with ideal Couette state at both endcaps (left panel of Fig. 4, the end effect is removed completely by enforcing ideal Couette state at both endcaps, thus no Ekman circulation is present) to 21.7 s^{-1} with two rings just as in the real experiment (right panel of Fig. 4). This is due to the residual magnetic Ekman circulation, which modifies the background flow. Also as pointed out in Liu (2008b), the linear growth rate of an absolute instability in a bounded geometry is reduced by the "absorping" end plate, with the reduction extent proportional to $O(\Gamma^{-2})$, where the aspect ratio is $\Gamma = h/(r_2 - r_1)$ and h is the height of the cylinders (see Fig. 1).

Interestingly the linear growth rate with ideal Couette state at both endcaps (right panel of Fig. 4) matches the growth rate of the fastest growing mode, which naturally is the dominant mode, got from a linear code developed by (Goodman & Ji 2002), in which vertical periodicity is assumed, but the radial equations are solved directly by finite differences with perfectly insulating boundary conditions (Table 2). The agreement suggests that viscous effects are slight, since the no-slip conditions on the horizontal velocities at the endcaps differ from the periodicity imposed by the linear code.

2.2. Strong Magnetic Field Suppresses MRI with Two Split Rings

MRI essentially is a weak field instability. It is characteristic of MRI for a strong magnetic field to suppress this instability. Our experimental facility can only allow $I_\varphi \lesssim$ 1200 A. Thus we need to try carefully to find one set of proper parameters under which one growing mode is present with low I_φ while absent with larger I_φ. Fig. 5 demonstrates this property for simulations in which the boundary rotation rates $(\Omega_1, \Omega_2, \Omega_3, \Omega_4)$ are scaled to 45% of their designed values (Table.1).

3. Nonlinear Saturation

3.1. Inflowing "Jet" Observed near the Middle Plane

For $Re = 6400$, the final state is not steady. Typical time averaged flow and field patterns are shown in Fig. 6. The poloidal flux and stream functions are defined so that

$$\boldsymbol{V}_P \equiv V_r \boldsymbol{e}_r + V_z \boldsymbol{e}_z = r^{-1} \boldsymbol{e}_\varphi \times \boldsymbol{\nabla} \Phi, \qquad \boldsymbol{B}_P \equiv B_r \boldsymbol{e}_r + B_z \boldsymbol{e}_z = r^{-1} \boldsymbol{e}_\varphi \times \boldsymbol{\nabla} \Psi, \qquad (1)$$

which imply $\boldsymbol{\nabla} \cdot \boldsymbol{V}_P = 0$ and $\boldsymbol{\nabla} \cdot \boldsymbol{B}_P = 0$. The divergence of the velocity field in these compressible but subsonic simulations is nonzero but small.

We note that the induced toroidal field is around 6% of the initial axially imposed magnetic field at this magnetic Reynolds number $Re_{\rm m}$: $B_{\varphi,\max} \approx 0.06 B_\infty$. The most striking feature is the inflowing "jet" centered near $z = 13.95$ cm in Fig. 6 (see also Fig. 7), which is opposite to the usual Ekman circulation (Kageyama et al. 2004). It seems that the rapid outflowing "jet" found in (Liu et al. 2006b) with vertically periodic boundary condition, where the position of the "jet" is arbitrary, is shifted to the boundary layer, near the end caps in the experiment.

The inward "jet" near the inner cylinder part is a direct consequence of MRI. For MRI-stable regimes, Liu (2008a) discuss the influence of independently controlled split endcaps upon the poloidal circulation and the influence of the axial magnetic field and Reynolds number upon the Stewartson and Ekman layers. In such regimes, an *outflowing* jet occurs near the inner cylinder, in our apparatus, as it does in purely hydrodynamic Ekman circulation (i.e., $\Lambda = 0$). However in the MRI-unstable regime for the same Elsasser number Λ, the middle clock-wise cell enlarges both horizontally and vertically and eventually dominates the other cells, which retreat to the corners if the instability is strong enough. This leads to one inflowing "jet" near the inner cylinder (Fig. 7).

Further evidence that MRI causes the inflowing jet was found in simulations with the

ideal Couette state imposed at the end caps, to remove Ekman circulation (Fig. 8). Fig. 8 shows a clear inflowing jet near the inner cylinder in this case (see also Fig. 9). This suggests that the poloidal circulation seen in the final state in the split-endcap cases (Fig. 6 (b)) is caused solely by saturation of MRI rather than (magnetically modified) Ekman circulation.

3.2. MRI Enhances Radially Outward Angular Momentum Transport at Saturation

Astrophysicists are interested in the angular momentum transport due to MRI since MRI is supposed to be the most probable mechanism to explain the fast accretion in the astrophysical disks. Fig. 10 displays the time-averaged r-profiles of the radial advective, viscous, and magnetic torques, i.e. the angular momentum fluxes integrated over cylinders coaxial with the boundaries:

$$\Gamma_{\text{advective,r}}(r) = 2\pi \int_0^h dz \, \rho r^2 v_r v_\varphi \,, \tag{2}$$

$$\Gamma_{\text{magnetic,r}}(r) = 2\pi \int_0^h dz \left(-\frac{r^2 B_r B_\varphi}{4\pi} \right) \,, \tag{3}$$

$$\Gamma_{\text{viscous,r}}(r) = 2\pi \int_0^h dz \left[-r^3 \rho \nu \frac{\partial}{\partial r} \left(\frac{v_\varphi}{r} \right) \right] \tag{4}$$

$$\Gamma_{\text{total,r}}(r) = \Gamma_{\text{advective,r}}(r) + \Gamma_{\text{magnetic,r}}(r) + \Gamma_{\text{viscous,r}}(r) \,, \tag{5}$$

where dr and dz are the radial and vertical cell sizes respectively.

In contrast to the final state for vertically periodic boundary conditions (Liu et al. 2006b), the total radial torque is not constant with radius. Since our numerical scheme conserves angular momentum exactly, we can infer a vertical flux arising from exchange of angular momentum with the endcaps (see also Fig. 11). In the statistical steady state (nonlinearly saturated final state) the sum of the angular momentum flux on all boundaries should be zero, at least on time average. In this case it is fluctuating since the final state is not steady given high Reynolds number. From the gradients of the radial torque, we identify four Ekman circulation cells: where $d\Gamma_{\text{total,r}}/dr > 0$ (< 0) , the fluid is losing (gaining) angular momentum at the endcaps and the boundary-layer flow is therefore radially inward (outward). This is consistent with the discussion in Liu (2008a) of the poloidal circulation driven by two split rings. The radial magnetic and advective torques vanish at r_1 and r_2 because of the boundary conditions but are important at intermediate radii, especially the advective. All components of the radial torque are positive, which means that the angular momentum is transported radially outwards.

Fig. 11 displays the time-averaged r-distributions of the vertical total angular momentum flux at both endcaps $(z = 0, h)$:

$$\Gamma_{\text{advective,z}}(r, z = 0, h) = 2\pi \int_{r_1}^{r} dr \rho r^2 v_z v_\varphi \,, \tag{6}$$

$$\Gamma_{\text{magnetic,z}}(r, z = 0, h) = 2\pi \int_{r_1}^{r} dr \left(-\frac{r^2 B_z B_\varphi}{4\pi} \right) \,, \tag{7}$$

$$\Gamma_{\text{viscous,z}}(r, z = 0, h) = 2\pi \int_{r_1}^{r} dr \left[-r^2 \rho \nu \frac{\partial}{\partial z} (v_\varphi) \right] \,. \tag{8}$$

Since at both endcaps, both the advective and magnetic angular momentum fluxes are zero due to the boundary conditions, the total angular momentum at both endcaps $\Gamma_{\text{total,z}}(r, z = 0, h) = \Gamma_{\text{advective,z}}(r, z = 0, h) + \Gamma_{\text{magnetic,z}}(r, z = 0, h) + \Gamma_{\text{viscous,z}}(r, z = 0, h)$ are simply the viscous angular momentum flux $\Gamma_{\text{viscous,z}}(r, z = 0, h)$.

From these two figures, we can see that the global angular momentum is entering from the inner cylinder then most of it is flowing out from the outer cylinder while the rest of it is flowing out at the two end caps. *Angular momentum is transported radially outward.*

It is very interesting to derive the dependence of the total torque at the inner cylinder, which is mainly responsible for driving the rotation, and of the sum of the vertical torques at both endcaps, on Reynolds number (Re). From Fig. 12 (a), we infer the following scalings (100% run, $Re_{\text{m}} = 16$):

(1) In the absence of magnetic field (100% run, $100 \lesssim Re \lesssim 25600$),

$$\Gamma_{\text{initial},r}(r_1) \approx 2.69 \times 10^4 Re^{-0.691} \,; \tag{9}$$

These hydrodynamic states (rather than ideal Couette flow) will be used as the initial conditions for the MRI experiments. The maximum relative error ratio, defined as the ratio of the absolute difference of the value from the simulation and the fitted value (Eq. 9) over the former one, is $\lesssim 0.4\%$.

(2) For $I_\varphi = 1000$ A and $\Lambda = 0.36$ (100% run, $100 \lesssim Re \lesssim 25600$).

$$\Gamma_{\text{final},r}(r_1) \approx 1.98 \times 10^4 Re^{-0.639} \,. \tag{10}$$

This corresponds to the final states of the MRI experiment. The maximum relative error ratio is $\lesssim 0.3\%$. From these two scaling laws, *the MRI indeed enhances the angular momentum transport at saturation, though slightly* (see discussion below). The enhancement is far beyond the arrange of the error bar (see the error bars on panel (a) of Fig. 12). It is reasonable for Γ_r in both magnetized and unmagnetized cases to decrease with increasing Re since

the viscous coupling to the walls scales as $Re^{-1/2}$ in standard unmagnetized Ekman layers (*i.e.* the endcaps are corotating solidly with the outer cylinder). In this more complicated case (with split rings), we also expect a similar relationship, though the magnetized Ekman and Stewartson layers complicate the problem (Liu 2008a).

If Eq. 9 and Eq. 10 also work at larger Reynolds numbers, so that they may safely be extrapolated to the experimental Reynolds number ($Re \approx 1.15 \times 10^7$, 100% run), then the total radial torque of the initial and final state at the inner cylinder may be as large as

$$\Gamma_{\text{initial},r}(r_1) \approx 0.359 \text{ [Newton m]} \tag{11}$$

and

$$\Gamma_{\text{final},r}(r_1) \approx 0.611 \text{ [Newton m]} \tag{12}$$

respectively. Thus, the ratio of the increase of the torque over the initial torque is: $(0.611 - 0.356)/0.356 = 72\%$, which is quite measurable and indicates that at the experimental Reynolds number MRI would dominate the residual magnetic Ekman circulation in the point of view of transporting the angular momentum. There are, however, reasons for caution in accepting this estimate. For example, the experimental flow may be three-dimensional and turbulent, which might result in an even higher torque in the final state, and the absolute values of both the exponents seem to decrease at larger Reynolds number and the difference of these two exponents is small. These concerns all make the extrapolation of Eq. 9 and Eq. 10 to the experimental Reynolds number a bit risky. Nevertheless, we expect a noticeable torque enhancement in the MRI-unstable regime.

From Fig. 12 (b), we can see that: (1) At larger Reynolds number, $(\Gamma_z(z = 0) + \Gamma_z(z = h))/\Gamma_r(r = r_1)$ is increased, which means that larger part of the total angular momentum is transported vertically. (2) In the MRI stable regime ($Re \lesssim 1600$), the magnetic field enhances the vertical transport of the angular momentum. This is also reasonable since the magnetic field would align the flow, thus having the cells elongating and penetrating deeper into the bulk. The size of the middle cells is increased vertically by the residual magnetic Ekman circulation. These are consistent with the conclusions deduced in Liu (2008a). (3) In the MRI unstable regime ($Re \gtrsim 3200$), the onset of the MRI results in more angular momentum transported radially outwards and less vertically. The MRI would increase the scale of the middle cell horizontally. Therefore it transports more angular momentum radially outwards.

4. Conclusions

In conclusion of this paper we have simulated the nonlinear development of magnetorotational instability in a nonideal magnetohydrodynamic Taylor-Couette flow. The simulations mimic an on-going experiment except that the conductivity of the stainless steel walls is neglected and the simulation is started from an ideal Couette state rather than an actual hydrodynamic statistical steady state driven by split end caps. We have also restricted our study to smaller fluid Reynolds number (Re) than in the experiment, however we have used exactly the same magnetic Reynolds number (Re_{m}). MRI grows from small amplitudes at rates in good agreement with linear analyses without the end cap effects.

Concerning the MRI simulations with two split independently rotating rings like the real experimental facility, we draw the following conclusions:

1. A clear linear phase is observed; the linear MRI growth rate is reduced by the residual magnetized Ekman circulation.

2. Strong magnetic field suppresses MRI.

3. In the final state one inflowing "jet" opposite to the usual Ekman circulation "jet" (Kageyama et al. 2004) is found near the inner cylinder, a direct consequence of MRI rather than the residual Magnetic Ekman circulation (100% run).

4. The MRI enhances the angular momentum transport at saturation. (100% run).

5. The final state contains horizontal fields about 6% as large as the initial vertical field for $Re_{\mathrm{m}} \approx 20$ (100% run).

We emphasize that these conclusions are based on axisymmetric simulations restricted to the range $10^2 \lesssim Re, Re_{\mathrm{m}} \lesssim 10^{4.4}$ with the idealizations mentioned above. The simulation results considering the conductivity of the steel container, starting from an actual hydrodynamical equilibrium and the comparison with the experimental results would be given in a future paper.

REFERENCES

Balbus, S. & Hawley, J. 1998, Rev. Mod. Phys., 70, 1

Burin, M., Schartman, E., Ji, H., Cutler, R., Heitzenroeder, P., Liu, W., Morris, L., & Raftopolous, S. 2006, Exp. Fluids, 40, 962

Fleming, T. P., Stone, J. M., & Hawley, J. F. 2000, Astrophys. J., 457, 355

Gilman, P. 1971, Phys. Fluids, 14, 7

Goodman, J. & Ji, H. 2002, J. Fluid Mech., 462, 365

Hayes, J. C., Norman, M. L., Fiedler, R. A., Bordner, J. O., Li, P. S., Clark, S. E., ud Doula, A., & Low., M.-M. M. 2006, Astrophys, J. Suppl., 165, 188

Hollerbach, R. & Fournier, A. 2004, in MHD Couette Flows: Experiments and Models, American Inst. Phys. Conf. Proc., ed. G. Rosner, G. Rüdiger, & A. Bonanno, Vol. 733, 114–121

Hollerbach, R. & Rüdiger, G. 2005, Phys. Rev. Lett., 95, 124501

Ji, H., Burin, M., Schartman, E., & Goodman, J. 2006, Nature, 444, 343

Ji, H., Goodman, J., & Kageyama, A. 2001, Mon. Not. R. Astron. Soc., 325, L1

Kageyama, A., Ji, H., Goodman, J., Chen, F., & Shoshan, E. 2004, J. Phys. Soc. Japan., 73, 2424

Knobloch, E. & Julien, K. 2005, Mon. Not. R. Astron. Soc., 000, 1

Liu, W. 2008a, accepted by PRE

—. 2008b, in preparation

Liu, W., Goodman, J., Herron, I., & Ji, H. 2006a, Phys. Rev. E, 74, 056302

Liu, W., Goodman, J., & Ji, H. 2006b, Astrophys. J., 643, 306

—. 2007, Phys. Rev. E., 76, 016310

Noguchi, K., Pariev, V. I., Colgate, S. A., Beckley, H. F., & Nordhaus, J. 2002, Astrophys. J., 575, 1151

Priede, J., Grants, I., & Gunter, G. 2007, Phys. Rev. E, 75, 047303

Roach, A., Ji, H., Liu, W., & Goodman, J. 2007, in APS-DPP07, abstract BP8.00084

Rüdiger, G. & Hollerbach, R. 2007, Phys. Rev. E, 76, 068301

Rüdiger, G., Hollerbach, R., Schultz, M., & Shalybkov, D. 2005, Astron. Nachr., 326, 409

Rüdiger, G., Hollerbach, R., Stefani, F., Gundrum, T., Gerbeth, G., & Rosner, R. 2006, Astrophys. J., 649, L145

Sano, T. & Inutsuka, S. 2001, Astrophys. J., 561, L179

Sisan, D. R., Mujica, N., Tillotson, W. A., Huang, Y., Dorland, W., Hassam, A. B., Antonsen, T. M., & Lathrop, D. P. 2004, Phys. Rev. Lett., 93, 114502

Stefani, F., Gundrum, T., Gerbeth, G., Rüdiger, G., Schultz, M., Szklarski, J., & Hollerbach, R. 2006, Phys. Rev. Lett., 97, 184502

Stefani, F., Gundrum, T., Gerbeth, G., Rüdiger, G., Szklarski, J., & Hollerbach, R. 2007, New J. Phys., 9, 295

Szklarski, J. 2007, Astron. Nachr., 328, 499

Umurhan, O. M., Menou, K., & Regev, O. 2007a, Phys. Rev. E, 76, 036310

—. 2007b, Phys. Rev. Lett., 98, 034501

Velikhov, E. P., Ivanov, A. A., Lakhin, V. P., & Serebrennikov, K. S. 2006, Physics Letters A., 356, 357
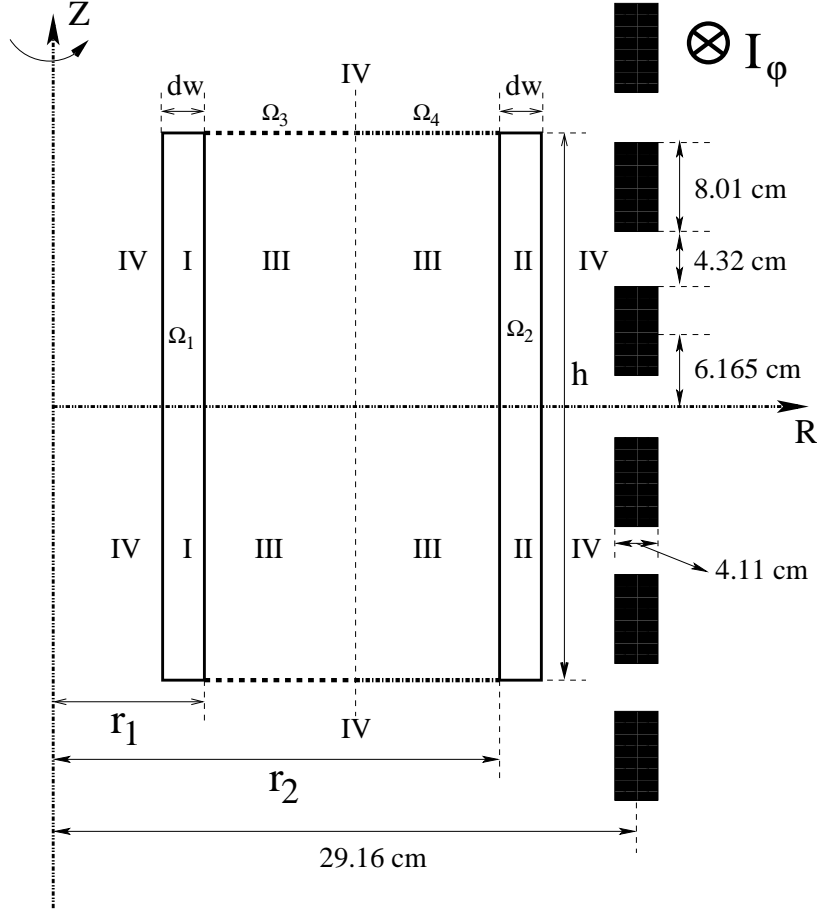
Fig. 1.— Computational domain for simulations of Princeton MRI experiment. Region (I): Inner steel cylinder, angular velocity Ω_1, magnetic resistivity η_I. (II): outer steel cylinder, Ω_2, η_{II}. (III): liquid gallium, η_{Ga}; (IV): vacuum. Thick dash line: insulating inner ring, Ω_3. Thick dash-dot line: insulating outer ring, Ω_4. Thin dash line: middle plane. Dimensions: radius of the inner cylinder, r_1; radius of the outer cylinder, r_2; height of the cylinders, h; thickness of inner and outer steel cylinder, $d_w = 0.9525\,\mathrm{cm}$; black rectangles, external coils.
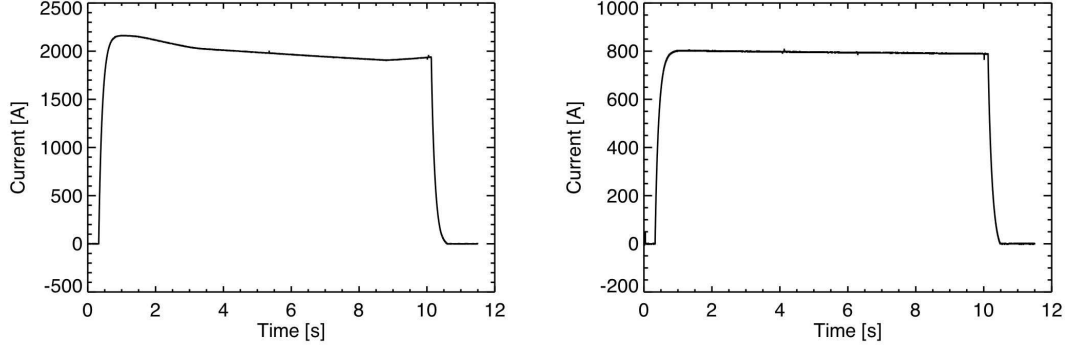
Fig. 2.— Figure Courtesy of Mark Nornberg. Experimental wave form of the coil current. Left panel: $I_\varphi = 1000$ A; right: $I_\varphi = 400$ A. Shown here is the total current in the general circuit. Since the six coils are split into two sets of three in parallel, with the upper three in series and the bottom three also in series, the current in the coils should be the one in the general circuit divided by 2.
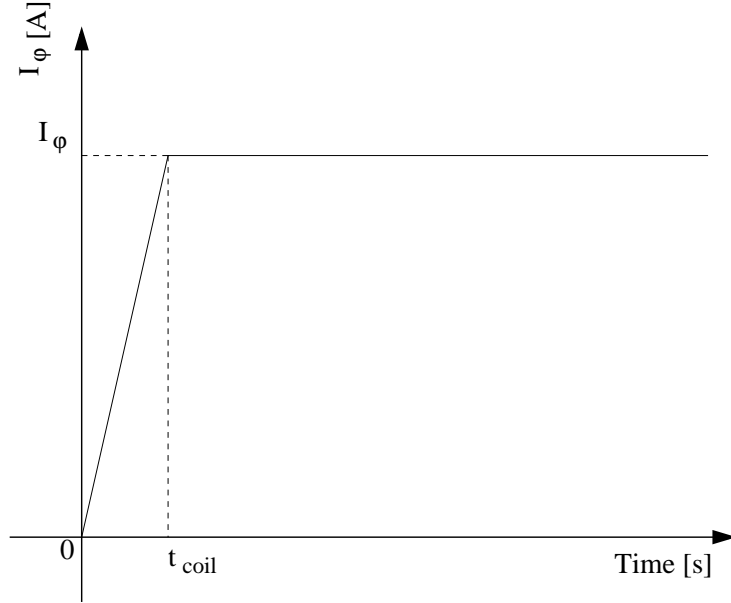
Fig. 3.— Simulated Current pattern in the external coils; the ramp time $t_{coil} = 0.2$ s; except where stated explicitly, the steady current $I_\varphi = 1000$ A.
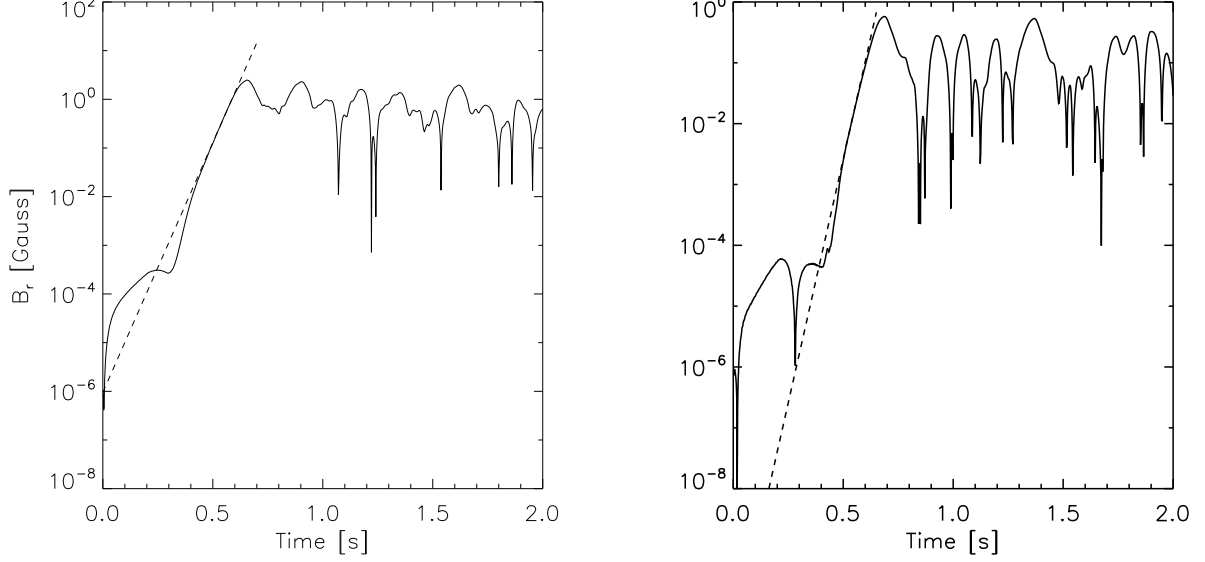
Fig. 4.— 100% run (MRI unstable) and $I_\varphi = 1000$ A. B_r vs. time for $Re = 6400$, $Re_\mathrm{m} = 20$ sampled outside the fluid at $z = 13.95$ cm, $r = 25.0$ cm. "Bottom end cap" is located at $z = 0$. Height $h = 27.9$ cm. Left panel: endcaps split into two rings, Growth rate $\gamma = 21.7$ s^{-1}; right panel: ideal Couette state at both endcaps, Growth rate $\gamma = 33.1$ s^{-1}.

Dimensions	
$r_1 = 7.1$ cm	$r_2 = 20.3$ cm
$h = 27.9$ cm	$d_w = 0.9525$ cm
Material Properties	
$\rho_\mathrm{Ga} = 6.35$ g cm^{-3}	$\eta_\mathrm{Ga} = 2.43 \times 10^3$ cm^2 s^{-1}
$\eta_\mathrm{Steel} = 5.73 \times 10^3$ cm^2 s^{-1}	$\sigma_\mathrm{Steel} = 1.25 \times 10^{16}$ s^{-1}
Rotation Profile (100% run)	
$\Omega_1/2\pi = 4000$ rpm	$\Omega_2/2\pi = 533$ rpm
$\Omega_3/2\pi = 1820$ rpm	$\Omega_4/2\pi = 650$ rpm
Rotation Profile (45% run)	
$\Omega_1/2\pi = 1600$ rpm	$\Omega_2/2\pi = 239.85$ rpm
$\Omega_3/2\pi = 819$ rpm	$\Omega_4/2\pi = 292.5$ rpm

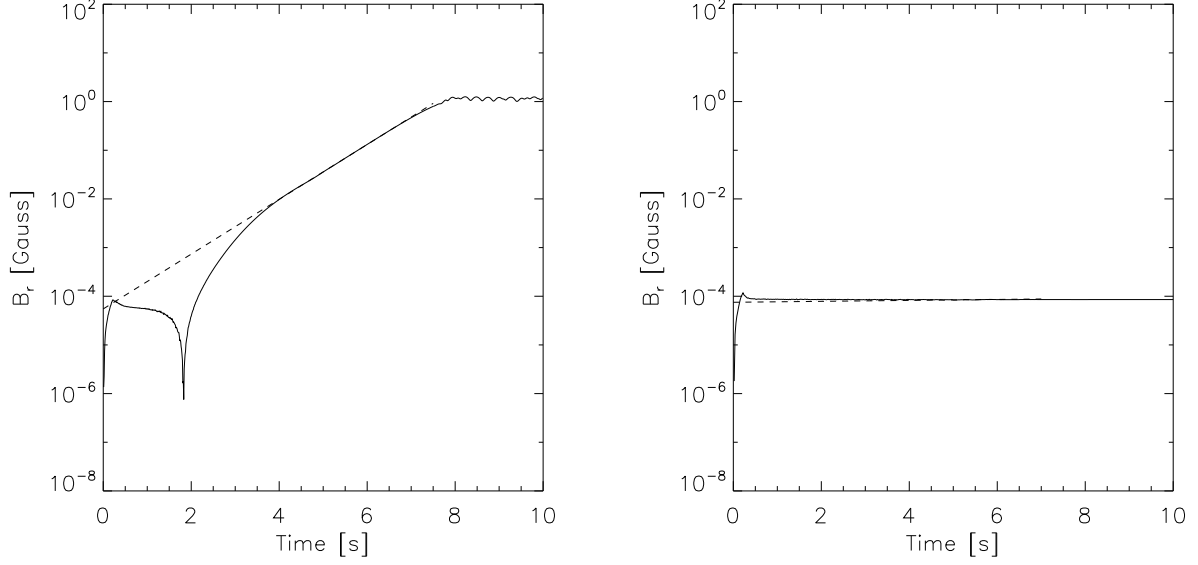Table 1: Parameters in Gaussian units used in the simulations

Fig. 5.— 45% run. B_r *vs.* time for $Re = 6400$, $Re_\mathrm{m} = 7.3$ sampled outside at $z = 13.95$ cm, $r = 25.0$ cm. "Bottom end cap" is located at $z = 0$. Height $h = 27.9$ cm. left panel: $I_\varphi = 750$ A, growth rate $\gamma = 1.3$ s^{-1}; right panel: $I_\varphi = 1200$ A, stable.

Re_m	Re	n	Prediction $[\mathrm{s}^{-1}]$	Simulation $[\mathrm{s}^{-1}]$
16	6400	1	33.7	33.1
16	6400	2	13.8	

Table 2: 100% run. Growth rates from semianalytic linear analysis *vs.* simulation.
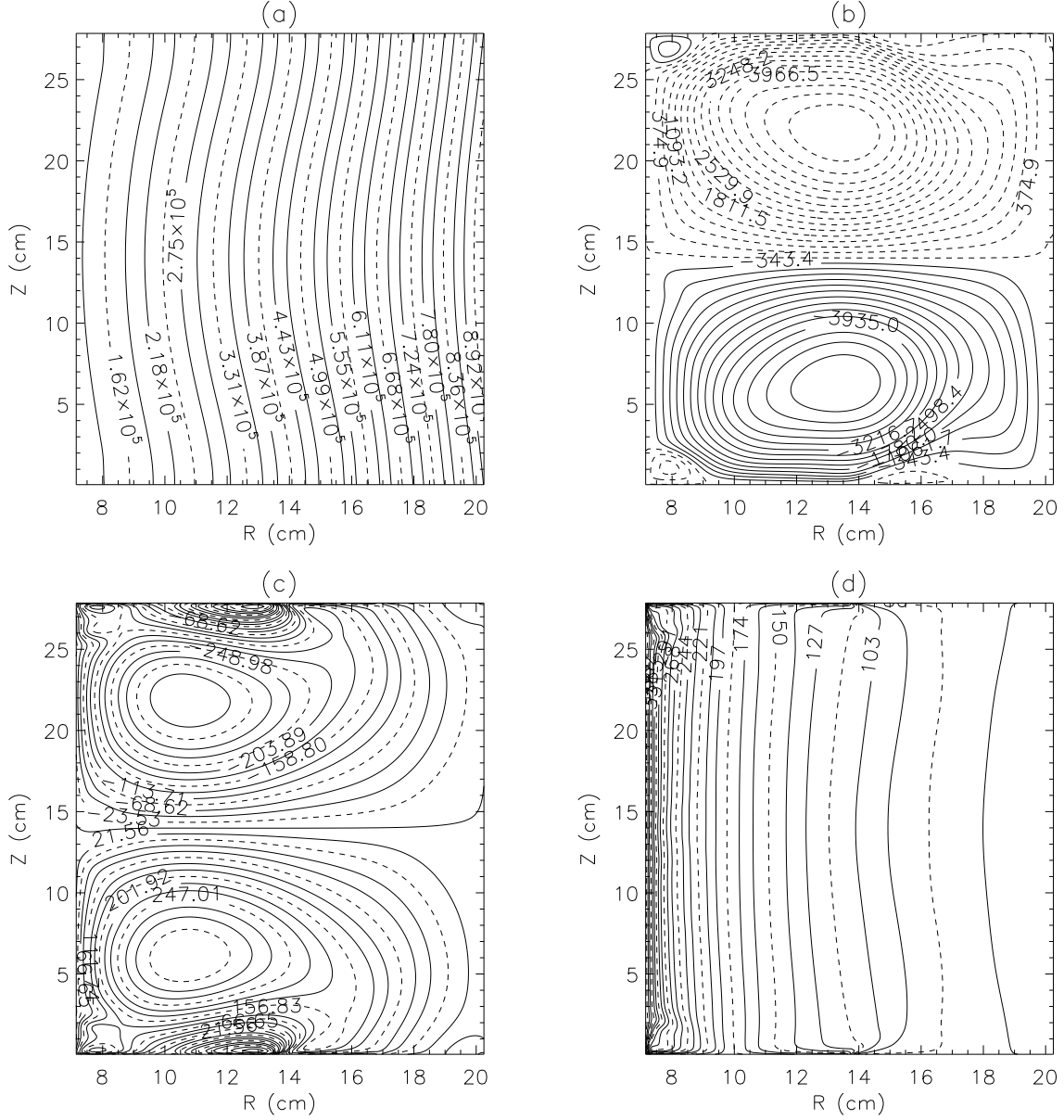
Fig. 6.— 100% run. Contour plots of final-state velocities and fields (MRI unstable). $Re = 6400$, $Re_{\rm m} = 20$. $I_\varphi = 1000$ A, $\Lambda = 0.36$. (a) Poloidal flux function Ψ (Gauss cm^2) (b) Poloidal stream function Φ (cm^{2}s^{-1}) (c) toroidal field B_φ (Gauss) (d) angular velocity $\Omega \equiv r^{-1}V_\varphi$ (rad s^{-1}). In panel (b), dashed line indicates the clock-wise poloidal circulation while solid line indicates the anti-clock-wise poloidal circulation.
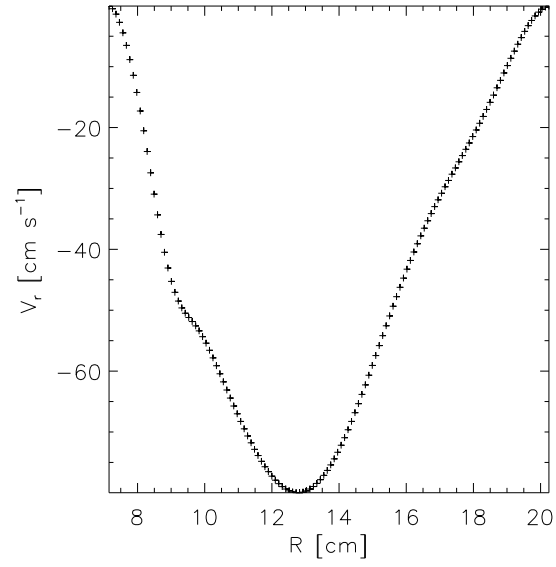
Fig. 7.— Corresponding to Fig. 6(b). 100% run (MRI unstable). Time averaged v_r *vs.* radius r on the midplane ($z = h/2$). $Re = 6400$, $Re_{\mathrm{m}} = 20$. $I_\varphi = 1000$ A, $\Lambda = 0.36$.
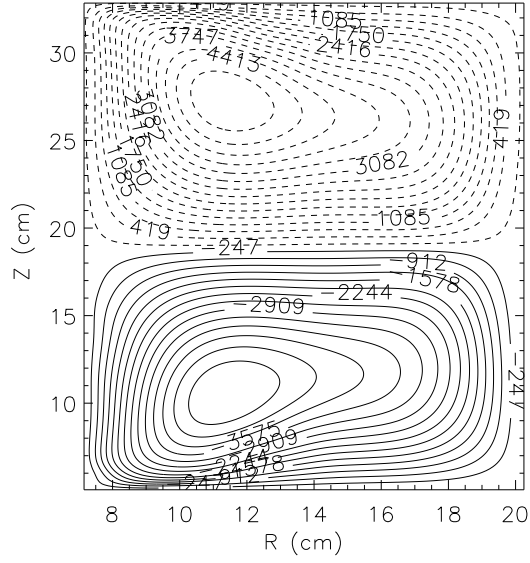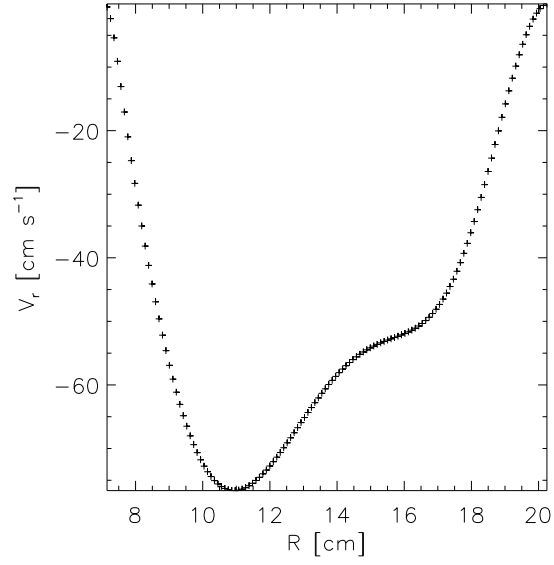
Fig. 8.— 100% rotation run (MRI unstable). Contour plots of poloidal stream function $\Phi \, (\mathrm{cm^2 s^{-1}})$ for $Re = 6400$ with ideal Couette state at the end caps. $I_\varphi = 1000$ A, $\Lambda = 0.36$. Dashed line indicates the clock-wise poloidal circulation while solid line indicates the anti-clock-wise poloidal circulation.

Fig. 9.— Corresponding to Fig. 8. 100% rotation run (MRI unstable). Time averaged v_r vs. radius r on the midplane ($z = h/2$) for $Re = 6400$ with ideal Couette state at the end caps. $I_\varphi = 1000$ A, $\Lambda = 0.36$.
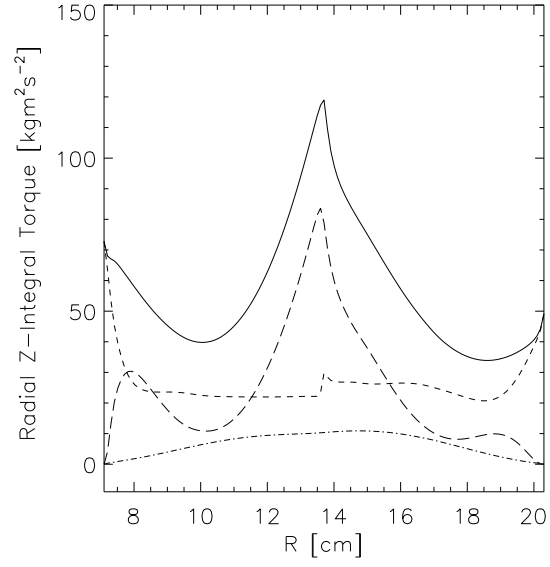
Fig. 10.— 100% run (MRI unstable). Time averaged z-integrated radial angular momentum fluxes versus r at saturation. $Re = 6400$, $Re_\mathrm{m} = 20$. $I_\varphi = 1000$ A, $\Lambda = 0.36$. Dash line , viscous torque; dash dot line , magnetic torque; long dash line , advective torque; solid line, total torque.
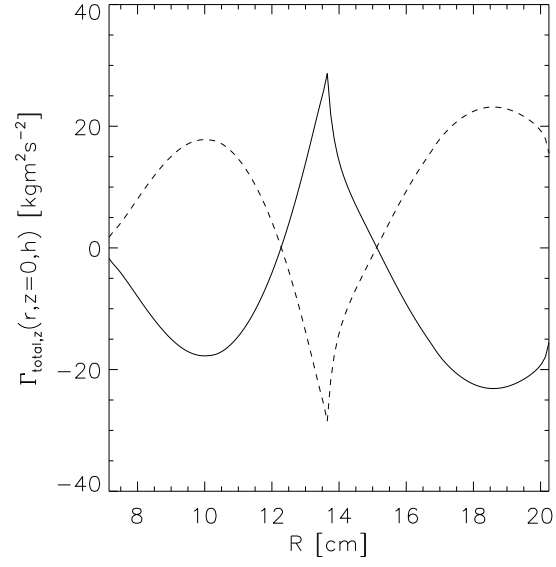
Fig. 11.— 100% run (MRI unstable). Time averaged vertical total angular momentum flux at both endcaps versus r at saturation. $Re = 6400$, $Re_\mathrm{m} = 20$. $I_\varphi = 1000$ A, $\Lambda = 0.36$. Solid line: bottom endcap ($z = 0$); dashed line: top endcap ($z = h$).
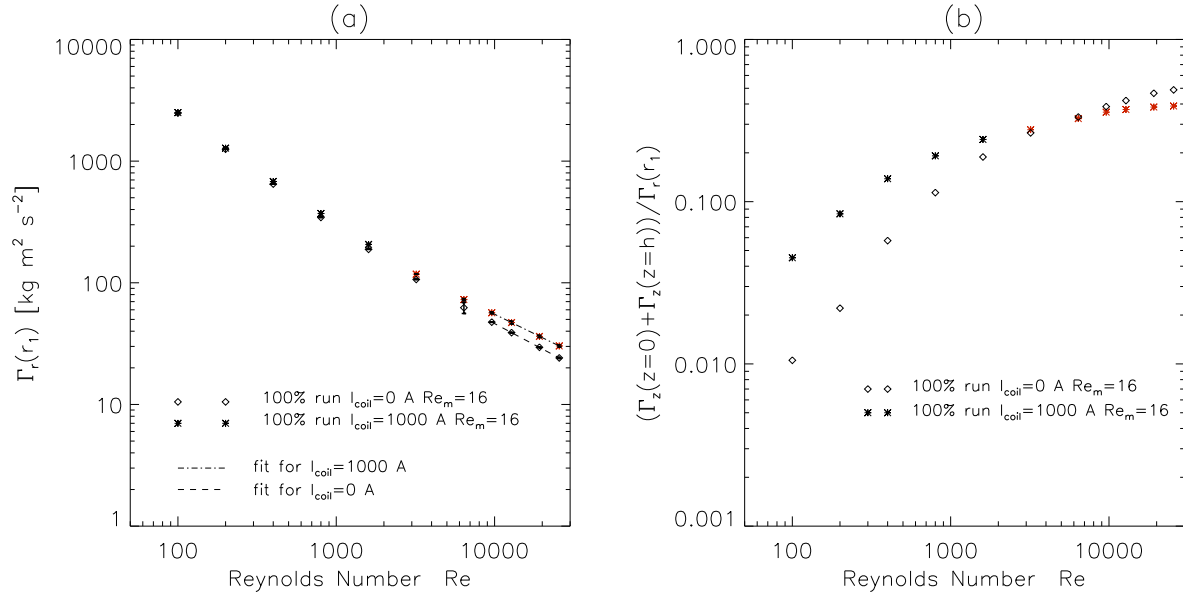
Fig. 12.— (Color) (a) Total radial torque at the inner cylinder (b) Sum of the total vertical torques at both endcaps *versus Re*. Note that in the simulations the magnetic diffusivity η is fixed to the experimental value $\eta = 2430$ cm^2 s^{-1} (Table.1), however the kinetic viscosity is varied for the purpose of extrapolation. In both panel, red colors: MRI unstable; black color: MRI stable. In panel (a), dashed lines have slopes of -0.691 (initial state) and dash-dot lines -0.639 (final state). The error bars on panel (a) (very small, typically $\sim 1\%$, hard to see on panel (a)) are the standard time-deviations. If $Re < 3200$, the error bars are zero in both magnetized and unmagnetized cases, which suggests the system is steady with low Reynolds number.